

Controlled growth and composition of multivariate metal-organic frameworks-199 via a reaction-diffusion process

Razan Issa^{1,§}, Fayrouz Abou Ibrahim^{1,§}, Mazen Al-Ghoul^{1,2} (✉), and Mohamad Hmadeh¹ (✉)

¹ Department of Chemistry, American University of Beirut, P.O.Box 11-0236, Riad El-Solh 1107 2020, Beirut, Lebanon

² Department of Chemistry, McGill University, 801 Sherbrooke Street West, Montreal H2A 0B8, Canada

[§] Razan Issa and Fayrouz Abou Ibrahim contributed equally to this work.

© Tsinghua University Press and Springer-Verlag GmbH Germany, part of Springer Nature 2020

Received: 4 February 2020 / Revised: 17 April 2020 / Accepted: 9 May 2020

ABSTRACT

In this paper, we exploit our prior successful synthesis of MOF-199 single crystals using the reaction-diffusion framework (RDF), to synthesize multivariate metal-organic frameworks (MTV-MOFs) version with enhanced properties. The MTV-MOFs are synthesized by creating defects within the MOF-199 crystal structure by integrating organic linkers entailing different functional groups. Accordingly, 5-aminoisophthalic acid (NH₂-BDC) and 5-hydroxyisophthalic acid (OH-BDC) are separately mixed with 1,3,5-benzenetricarboxylic acid (BTC) in three different starting ratios of X-BDC:BTC (1:3, 1:1) and 3:1). The effects of this linker on the morphology of the synthesized MTV-MOFs, their thermal stability, and their surface area are investigated. The extent of the incorporation of the linkers in the framework is elucidated via ¹H-NMR spectroscopy and it is shown that the incorporation varies as a function of the location along the tubular reactor, a characteristic of RDF. The enhanced properties of the synthesized MTV-MOFs are further demonstrated by measuring its adsorptive capability for methylene blue (MB) and rhodamine B (Rh B) in aqueous solution, and compared with that of the as-synthesized MOF-199. The kinetic and thermodynamic studies reveal that MTV-MOFs with the ratio of X-BDC:BTC (1:1) exhibit the best uptakes of MB (263 mg/g) for X = OH and Rh B (156 mg/g) for X = NH₂. The adsorbents are also easily regenerated for three consecutive cycles without losing their efficiency. We finally demonstrate that MTV-MOFs can be designed to tune the dye removal selectivity and enhance the removal capacity of both MB and RhB in a binary aqueous solution of these dyes.

KEYWORDS

reaction-diffusion framework (RDF), multivariate metal-organic frameworks (MTV-MOFs), adsorption, methylene blue (MB), rhodamine B (Rh B)

1 Introduction

Metal-organic frameworks (MOFs) are an expansible class of highly crystalline porous extended networks [1]. They are hybrid materials formed by anchoring organic linkers subsuming mainly carboxylate moieties, with metal clusters via strong coordination bonds [2]. Many material scientists have focused their interests on designing new crystalline porous materials to fulfil highly specific functions and thus intended applications. MOFs are indeed modular structures and can be expanded by means of reticular chemistry to obtain ultrahigh porosity and surface area [3, 4]. MOF structures represent an epitome of versatile ultrahigh porous materials [5] and they have been extensively employed in a broad-range of applications especially in gas storage, catalysis, drug delivery, water purification and sensing [6–9]. The conspicuous interest in these hybrid materials does not rely back to its high surface areas only, but also to the immense number of metal salts and organic linkers that could be incorporated in the synthesis process [10]. Such diverse combinations of the reagents produce an indefinite number of MOFs exhibiting superior features and unique properties that precede vigorously other materials of pure organic or inorganic nature, including zeolites and activated carbon [11, 12]. More importantly, it is evident that the characteristics and the

properties of MOFs depend intensely on the synthesis route including the temperature of the reaction, proportions of the metal ions and the organic linkers with respect to each other, in addition to the nature and the extent of the solvents utilized [13]. Aided with these scenarios, material scientists are urged to upsurge their efforts in finding possible ways to optimize the physio-chemical properties of MOFs and reach the ultimate efficiency when targeted specific applications [14].

One suggested approach that serves as a potential platform for enhanced MOFs' physical and chemical properties is reached by mixing metals [15, 16] or incorporating more than one type of organic linkers [17] having different functionalities within the same framework [18], leading to structures known as multivariate MOFs (MTV-MOFs) [19, 20]. The intentions behind synthesizing MTV-MOFs is to generate versatile porous material that exclusively display dual opposing properties, create defects while conserving the entire framework and adjust the pore environments via allocating the functional groups into the framework at the preferred locations [21]. Such schemes owe to influence the properties of the single ligand MOFs and thus enhance its performance at the application level [22, 23]. The resulted heterogeneity within order in these MTV-MOFs depicts improvements in the adsorptive and catalytic properties [24–26]. Mainly, the linkers that are

Address correspondence to Mohamad Hmadeh, mohamad.hmadeh@aub.edu.lb; Mazen Al-Ghoul, mazen.ghoul@aub.edu.lb

mixed within the same framework have geometric similarities such as the length of the carbon chain [27]. Meanwhile incorporating linkers having different functional groups is a matter of challenge as the obtained material might lack a homogeneous single phase of the mixed linkers or lose its crystalline order [28]. However, some reports suggest possible routes for MTV-MOFs synthesis including metals or ligands mixing in the initial preparation solution [26, 29], solvothermal reaction [30], mechanochemical reaction [31], solvent-assisted linker exchange (SALE) [32, 33], sequential linker installation by post-synthetic modification [34, 35] or growing one MOF on the surface of another as core-shell structure [36, 37]. It is noteworthy to mention, that only very few reports have demonstrated the successful production of MOFs at room temperature [38–40].

The reaction diffusion framework (RDF) with the underlying coupling of chemical transformations, diffusion, crystal nucleation and growth [41–43] is a powerful tool for making crystalline material with a direct control of the crystal size and composition [39]. In RDF, reaction-diffusion systems can be exploited to form the solid material of interest by precipitating the involved reactants (co-precipitates) within a gel matrix by means of diffusion and without any other transport processes (Scheme 1) [44]. As the initially segregated reactants are diffused into each other, a resulting concentration gradient is established down the reaction tube. Such a gradient leads to higher nucleation rates and thus smaller crystals near the interface between the outer electrolyte solution (metal ions) and the agar-containing organic linkers, versus a dominant crystal growth regime characterized by larger crystals down the tube due to the relatively lower supersaturation [45, 46]. The gel plays a pivotal role in the three-dimensional crystal growth by avoiding sedimentation of crystals, eliminating convection, stabilizing the depletion zones around growing crystals, and retarding the rates of nucleation and growth. In our previous work, we took advantage of RDF and reported the controlled growth of MOF-199 at room temperature via the diffusion of copper ions through a gel matrix containing the 1,3,5-benzenetricarboxylic acid (BTC) [39].

Herein, we extend the success of RDF for the controlled synthesis of MTV-MOF-199 at room temperature by the diffusion of copper ions into a gel matrix containing BTC mixed with either 5-hydroxyisophthalic acid (OH-BDC) or 5-aminoisophthalic acid (NH₂-BDC) linkers at different ratios. Through a live monitoring of the crystal growth, we are capable of introducing spatial heterogeneity into MOF-199, while preserving its original crystalline network [28, 47, 48]. More

importantly, by using linkers entailing different functional groups, we are able to tune the defect in the MOF structure and the functional units within the pores. The diversity of the functional groups alters the physio-chemical properties of the structures and therefore their affinity to the guest molecules which is demonstrated here by testing the adsorptive activity of the synthesized MTV-MOFs-199 having their pores decorated either with hydroxyl or amino groups over methylene blue (MB) and rhodamine B (Rh B) dyes in an aqueous medium, and then comparing to the as-synthesized MOF-199 as well as other commonly used adsorbents such as activated carbon.

2 Experimental section

2.1 Synthesis of MTV-MOFs via RDF

2.1.1 Materials

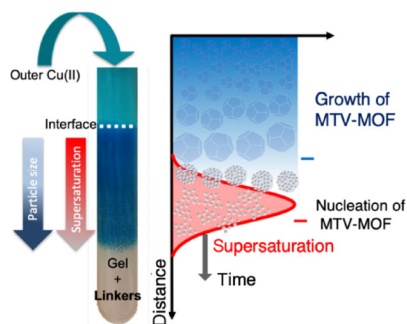
The chemical reagents, Cu(OAc)₂·H₂O and BTC were purchased from Acros Organics, agar gel from Bacto, OH-BDC, NH₂-BDC, N,N'-dimethyl formamide (DMF), dichloromethane (DCM) and ethanol absolute from Sigma Aldrich. All reagents were used as received and without any further purification.

2.1.2 Preparation procedure

MTV-MOFs were synthesized via RDF method in a Pyrex tube consisting of inner and outer mediums. The inner gel solution was prepared by dissolving mixture of X-BDC (OH-BDC or NH₂-BDC) and BTC (Scheme S1 in the Electronic Supplementary Material (ESM)), at three different starting molar ratios in a 1:1 ethanol/water solution (Table S1 in the ESM). Agar powder (1% w/w) was then added to the mixture, followed with a continuous heating and stirring until complete dissolution of the gel. Instantly, the mixture was poured into Pyrex tube, covered, and left to allow the complete congealing of the gel. By the time the inner had jellified, an outer solution constituting of copper acetate dissolved in a 1:1 ethanol:water mixture was poured on top of the congealed gel, allowing thereby the diffusion of electrolytes and the formation of MOF particles. The reaction-diffusion process of the system was kept for 72 h, after which the MOF precipitate was collected by dissolving the agar gel in hot water and then separating the crystals by centrifugation. Several washings by DMF were performed to eliminate the unreacted linkers. The MTV-MOF samples obtained were activated by solvent exchange with DCM and then dried under vacuum for 12 h.

2.2 Characterization

Powder X-ray diffraction (PXRD) patterns were recorded on a Bruker D8 Advance X-ray diffractometer using the Cu-K α radiation ($\lambda = 1.5406 \text{ \AA}$) at 40 kV and 40 mA. The morphology of MTV-MOFs was revealed by the scanning electron microscopy (SEM) images conducted on the FEI Quanta 600 FEG-SEM instrument. The Brunauer-Emmett-Teller (BET) surface areas of the MOF samples were calculated by the surface area analyzer (NOVA 2200e) after degassing the samples at 150° for 6 h. Thermogravimetric analysis (TGA) was obtained at a ramp rate of 5 °C/min from 30 to 700 °C under nitrogen atmosphere on NETZSCH TG 209F1 Libra TGA209F1D-0152-L. The amount of the linkers incorporated in the MOF structure was determined using BRUKER Advance NMR Spectrometer (500 MHz) after digesting the activated MOF in trifluoroacetic acid (TFA) and a deuterated dimethyl sulfoxide (DMSO). UV-Vis spectrophotometric measurements were performed on a Thermo Fisher Scientific Evolution Array spectrophotometer.



Scheme 1 Schematic representation of MTV-MOF synthesis via the reaction-diffusion framework in the tubular reactor. The copper solution (outer) is added on the top of a gel containing a mixture of the organic linkers. The supersaturation gradient (red curve) leads to a gradient in crystal sizes. Nucleation of the MTV-MOF takes place within the reaction zone (red region). Transition to multisized crystals with a gradient of linker composition takes place in its wake.

2.3 Organic dyes adsorption

In the adsorption experiments, 10 mg of the adsorbent (MOF) were added into 10 mL of solutions at different initial concentrations of the dyes, MB and Rh B, for 120 min (which was enough for the adsorption–desorption equilibrium to be established). The MOF samples underwent filtration prior to measuring the concentration of the equilibrium solution using UV spectrophotometry.

The amount of the organic dye adsorbed at equilibrium was calculated by the following equation

$$Q_e = \frac{(C_o - C_e)V}{W} \quad (1)$$

where C_o and C_e are the initial and the equilibrium concentrations (mg/L) of the dye respectively, V is the volume of the solution in liters (L), W is the mass of the MOF in grams (g) and Q_e is the adsorption capacity (mg/g) of the adsorbent at equilibrium. Similarly, the amount adsorbed of the dye at time t , was calculated using Eq. (2)

$$Q_t = \frac{(C_o - C_t)V}{W} \quad (2)$$

where C_t is the concentration (mg/L) of the dye at time t and Q_t is the adsorption capacity (mg/g) of the adsorbent at time t .

2.3.1 pH effect

In order to examine the effect of the pH on the adsorption process, 10 mg of the MOF sample were added to 10 mL of 3.20 ppm MB or 10 ppm of Rh B dye solution in five separate tubes at different pH ranging between 3 and 10. The pH values of 6.3 and 6.1 correspond to the MB and Rh B in deionized water without any additives, respectively. The initial solution's pH was adjusted through addition of NaOH or HCl.

2.3.2 Temperature effect

In order to perceive the effect of the temperature, the adsorption of MB and Rh B dyes by the MOF samples (MOF-199 and MTV-MOFs-199) was carried out at four different temperatures: 25, 35, 45 and 55 °C. The adsorption conditions for this task were 10 mg of the MOF, 10 mL of 3.20 mg/L of the dye for MB and 10 ppm for Rh B, and 120 min of contact time.

2.3.3 Kinetic study

The adsorption study was conducted at different contact times (1, 3, 5, 10, 15, 25, 30, 60 and 120 min) by adding 10 mg of the MOF sample into 10 mL of a 10 ppm of each dye solution. Aliquots of 0.25 mL were taken from each solution at a specific time and measured using the spectrophotometer after filtration of the adsorbent MOF.

2.3.4 Co-adsorption tests

In order to investigate the specificity of the introduced functional group towards each dye and their relative behavior when both dyes were present in solution, additional adsorption tests were done where 10 mg of the optimal systems OH-MOF-199 or NH₂-MOF-199 with 1:1 ratio were added to 10 mL of a 10 ppm Rh B or MB respectively and to 10 mL of a binary solution of 10 ppm of both Rh B and MB.

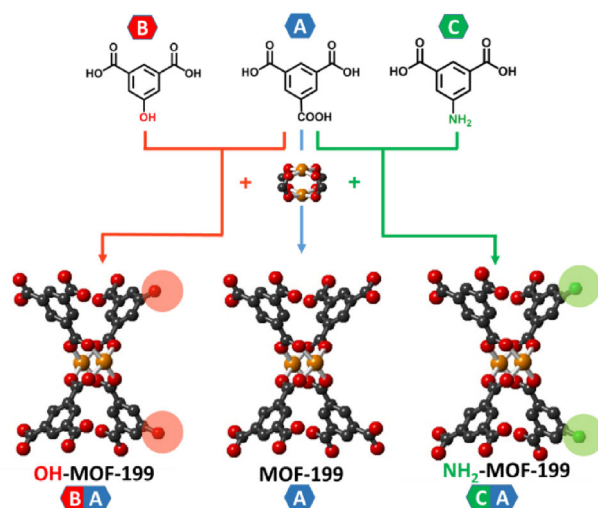
3 Results and discussions

3.1 Structural characterization of MOF-199 and its mixed linkers derivatives

MOF-199 and its mixed ligand derivatives (MTV-MOF-199)

were synthesized via RDF method in a Pyrex tube. BTC and OH-BDC or NH₂-BDC were mixed in three different ratios within the gel matrix to react with the diffused copper ions to form the crystals of MTV-MOF-199 (Table S1 in the ESM). The synthesis is summarized in Scheme 2. The collected crystals were then subjected to powder X-ray diffraction to confirm the phase purity of the samples.

The PXRD patterns for the MTV-MOFs-199 are compared to that of MOF-199 (Fig. 1). It is clear that these patterns are highly resolved and match perfectly with the theoretical profile of MOF-199 with no additional peaks. This indicates that the synthesized MTV-MOFs-199 are highly crystalline and pure with a single phase regardless of the ratio of the linkers. However, there's a slight peak broadening observed in the MTV-MOFs-199 profiles that is becoming more noticeable as the ratio of the introduced linker increases, and further indicating the decrease in the crystal size as well as a slight decrease in the overall crystallinity [49] manifested by a relative change in the peaks intensity. However, in the presence of high concentration of NH₂-BDC linker, new minor peaks appear in the XRD pattern of NH₂-MOF-199 (3:1) at 8.1°, 18°, and 26.6° which were obtained as well in a related study [26]. Further experiments were performed to investigate the cause of the extra peaks. It turned out that NH₂-BDC when introduced alone in the same synthesis conditions forms hierarchical structures with a very low crystallinity (Fig. S1 in the ESM) having the same peaks position appearing in the XRD pattern of NH₂-MOF-199 (3:1) while OH-BDC alone does not form any precipitate. It is worthy to note that a closer look at the PXRD of the crystals extracted from consecutive bands shows that this impurity forms only in the last band of



Scheme 2 Schematic presentation of the synthesis of MOF-199 and its mixed linkers derivatives through reacting Cu-paddle wheels with BTC linkers and OH-BDC or NH₂-BDC while preserving the original MOF-199 crystal order.

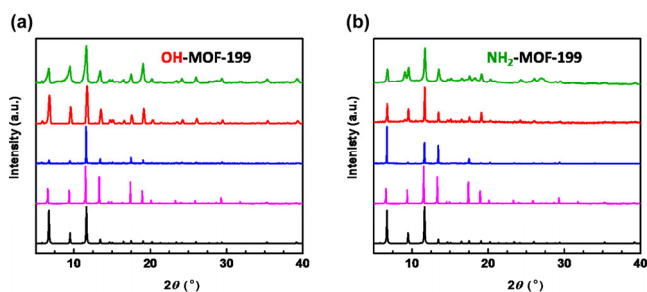


Figure 1 PXRD patterns of OH-BDC:BTC systems (a) and NH₂-BDC:BTC systems (b); calculated MOF-199 (black), synthesized MOF-199 (pink), (1:1) (blue), (1:1) (red) and (3:1) (green).

the tube hence the majority of the MTV-MOF-199 formed is pure (Fig. S1 in the ESM).

3.2 Effect of varying the ratios of the linkers on the morphology of the MOF

In order to investigate the morphology and further confirm the phase purity of the samples, the PXRD shown in Fig. S1 in the ESM as well as the SEM images of crystals extracted from three consecutive bands of the reaction tubes were recorded and representative images are shown in Fig. 2 and Table S2 in the ESM. The obtained images reveal one of main features of RDF which is the ability to lively monitor the growth and evolution of the crystals relative to the distance from the interface. As shown in Fig. 2, each tube is divided into three consecutive bands of equal width (band 1, band 2 and band 3). The nearest to the gel-outer solution interface is band 1. The SEM images display the progress of crystal growth in each MOF sample. As it can be clearly seen, band 1 contains the smallest crystals which is consistent with the dominance of nucleation near the interface where supersaturation is the highest. As we go down in the tube, crystal growth begins to take over, and crystals become larger in size with more defined shapes and edges. In the case of pure MOF-199, when no functionalized X-BDC was added in the reaction system, it can be seen that all the crystals in all bands are cubes with $6 \times \{100\}$ facets. When OH-BDC was introduced into the system in a OH-BDC:BTC ratio of 1:3, in the region close to the interface, the particle morphology changed to a cuboctahedron consisting of $6 \times \{100\}$ and $8 \times \{111\}$ facets. Away from the interface, the facets of $\{111\}$ become larger and the cuboctahedron is transformed to octahedron. However, when we increased the starting concentration of OH-BDC (OH-BDC:BTC (1:1 or 3:1)), interconnected spheres were formed which is consistent with highly defected frameworks. The interconnection between the particles could be responsible for the mesoporous behavior of the material. Likewise, in the case of the amino-functionalized MOF-199, relatively large cuboctahedral crystals were obtained for NH_2 -BDC:BTC (1:1 and 1:3). Interestingly, for higher starting ratio NH_2 -BDC:BTC (3:1), a hierarchical structure (Fig. S1 in the ESM) can be observed which could explain the mesoporous behavior and the decrease in the surface area.

The nitrogen adsorption isotherms corresponding to the MTV-MOFs having BTC in excess X-BDC:BTC (1:3) exhibit Type I isotherm similar to that of MOF-199, with a surface area of 900 and 800 m^2/g for OH-BDC and NH_2 -BDC, respectively (Fig. 3). It is worthy to note that when we increased

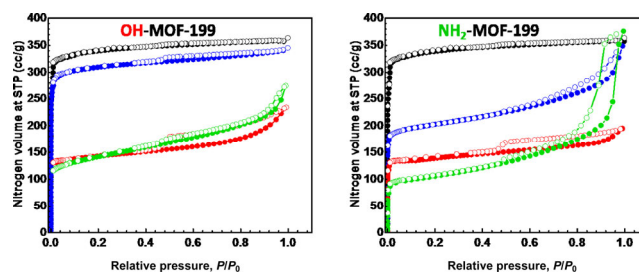


Figure 3 Nitrogen adsorption isotherms of OH-BDC:BTC systems (a) and NH_2 -BDC:BTC systems (b); MOF-199 (black), (1:3) (blue), (1:1) (red) and (3:1) (green).

the concentration of X-BDC to equate that of BTC (1:1), the obtained isotherm revealed a deviation from type I to type IV (Fig. 3), where the nitrogen uptake is high at high pressures indicating the formation of multilayers. In addition, the presence of the hysteresis loop at high relative pressures signifies the presence of mesopores. Meanwhile, at low P/P_0 , the flat plateau is indicative of a microporous behavior and the closure of the hysteresis loop at a P/P_0 value of around 0.4 signifies the existence of small mesopores. The calculated surface areas are 420 and 410 m^2/g for the hydroxyl-functionalized OH-MOF-199 and amino-functionalized NH_2 -MOF-199, respectively, which are much lower than that of the as-synthesized MOF-199. Seemingly, this decrease in surface area is associated with the decrease in the total pore volume (Table S3 in the ESM) upon the introduction of the new functional groups into the MOF framework and it is a common consequence for the formation of mesopores because the introduced linkers have lower coordination groups than BTC hence they play the role of breaking a wall between adjacent pores and combining them to give large pores [50, 51]. The obtained pore size distribution data are shown in Fig. S2 in the ESM. By further increasing the concentration of OH-BDC and NH_2 -BDC to exceed that of BTC at a ratio of 3:1, a slight disappearance of the hysteresis loop was observed, which suggests that there is a change in the pore size distribution inflicted by the major shape change of the material due to the domination of defects within the MOF-199 structure. This in turn results in the disappearance of the micropores and the lowering of the surface area to 360 and 400 m^2/g for OH-BDC and NH_2 -BDC, respectively.

3.3 Thermal stability of the MTV-MOFs-199

In order to study the effect of the incorporation of functionalized linkers within the MOF-199 topology on its thermal stability, TGA analysis was performed on the synthesized

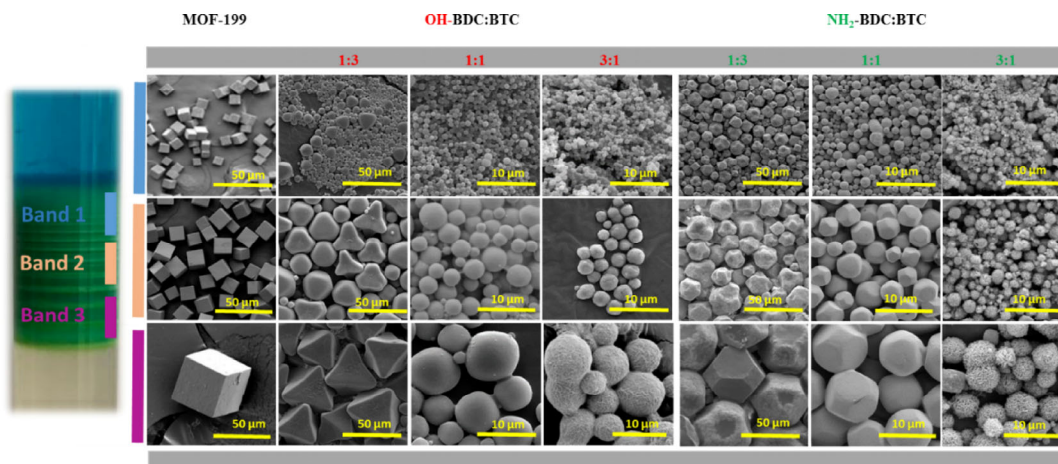


Figure 2 SEM images of the different MOF samples extracted from three consecutive bands of the reaction tubes.

solids and the obtained curves are shown in Fig. S3 in the ESM. It is clear that there is a slight decrease in the thermal stability of the MTV-MOFs-199 when compared to the as-synthesized MOF-199. This can be explained by a decrease in the number of Cu-paddle wheel secondary building units (SBUs) within the mixed linker MOFs. Nevertheless, the TGA profiles of MTV-MOFs-199 resemble that of MOF-199 where two main weight losses are observed. The first is at around 100 °C ranging from 5% to 20% weight loss resulting from the removal of the water molecules from the exposed metal sites of the SBUs. The second is near 300 °C with around 50% weight loss indicating the thermal decomposition of the MOF.

3.4 Evaluation of linker ratios in the MTV-MOFs

In order to validate the presence of OH-BDC and NH₂-BDC and to quantify the actual amount incorporated in the MOF structure, ¹H-NMR analysis of the digested crystals was conducted. The relative amount of the BTC, OH-BDC and NH₂-BDC linkers within the MOF structures was determined by the ratio of their peaks in the NMR spectrum. The results illustrated in Fig. 4 and Fig. S4 in the ESM, show that the final proportion of the linkers incorporated in the MOF structure is lower than the initial proportions used in the reaction mixture. The final amounts of OH-BDC and NH₂-BDC in each tube are calculated to be 32%, 26% and 16% for initial ratios of OH-BDC:BTC (3:1, 1:1 and 1:3) respectively, and 52%, 41% and 23% for initial ratios of NH₂-BDC:BTC (3:1, 1:1 and 1:3), respectively. This indicates that the amino functionalized linker is more efficiently incorporated in the MOF-199 structure. Furthermore, the RDF synthesis method allows us to calculate the extent of MOF-199 functionalization along the reaction tube and an interesting trend is obtained in all the studied systems where the amount of the functionalized linker incorporated decreases with decreasing supersaturation by going farther from the interface as shown in Fig. 4. In other words, the most defected MOF-199 can be extracted from the first bands for all systems. Representative NMR spectra are shown in Fig. S5 in the ESM. Further FT-IR studies done on a representative sample of the OH-BDC:BTC system are shown in Fig. S6 in the ESM. The latter displays a stretching vibration at around 1,640 cm⁻¹ corresponding to the -COOH groups of the BTC coordinated to copper metal ions, a broad band appearing within 3,500–2,700 cm⁻¹ signifying the presence of free -OH groups, and band appearing between 500–400 cm⁻¹ verifying the existence of the Cu–O bond.

3.5 Organic dyes adsorption

3.5.1 Adsorption isotherm

In order to demonstrate the importance of the functionalization and its resulting defects within MOF-199 structure, MTV-MOF-199 samples were employed as adsorbents for MB and

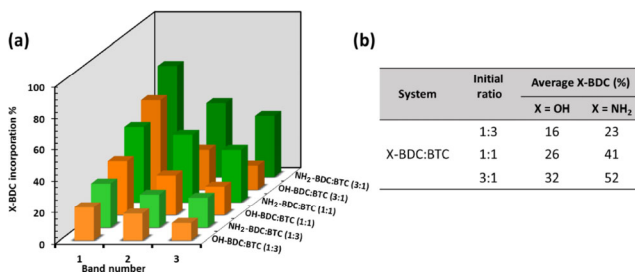


Figure 4 Percentages of OH-BDC (orange) and NH₂-BDC (green) incorporated within OH-MOF-199 and NH₂-MOF-199 crystals extracted from three consecutive bands (a) and their corresponding average values as a function of the starting ratios (b).

Rh B removal from water (Fig. 5).

The hydroxyl-functionalized version OH-MOF-199 shows high affinity toward MB; however, the amine-functionalized version NH₂-MOF-199 is found to be good adsorbent for Rh B. More importantly, both defected systems are found to be better adsorbents than MOF-199. In our study, the fit to a Langmuir isotherm is found to have the highest *R*-squared values compared to the Freundlich model as shown in Table S4 in the ESM. The plots in Fig. 6 are fitted in accordance to the non-linear form of the Langmuir isotherm equation

$$q_e = \frac{q_{\max} K_L C_e}{1 + K_L C_e} \quad (3)$$

where *K_L* is the Langmuir equilibrium constant (L/mg) and *q_{max}* is the monolayer adsorption capacity of the adsorbent (mg/g). It is clear from Table S4 in the ESM that the MTV-MOFs with starting ratios of OH-BDC:BTC (1:1) and NH₂-BDC:BTC (1:1) exhibit the highest *q_{max}* values of 263 and 156 mg/g for MB and Rh B, respectively, when compared to MOF-199 and other defected structures. Furthermore, fitting Langmuir model strongly suggests a physical adsorption process on the surface of the MOF crystals. Moreover, the maximum adsorption capacity of the newly synthesized MTV-MOFs efficiency was compared to numerous common adsorbent materials and is shown to perform better than many of them as shown in Table 1.

3.5.2 Effect of the initial pH of the solution

The pH of the solution is an imperative factor as it greatly influences the adsorption process in the aqueous solution mainly by altering the surface charge of the adsorbent and the charge state of the adsorbate. The corresponding adsorption experiments were conducted at different pH ranging between 3 and 10 and the results are shown in Fig. 7. When the pH is increased from 3 to 6, the adsorbed quantity of MB onto OH-BDC:BTC and Rh B onto NH₂-BDC:BTC increases until it reaches maximum values at the optimum pH (6.3 and 6.1)

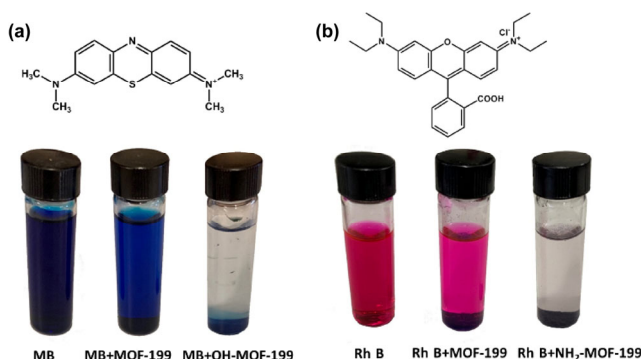


Figure 5 Adsorption of MB (a) and Rh B (b) dyes by the functionalized and defected MOF-199 compared to pure MOF-199.

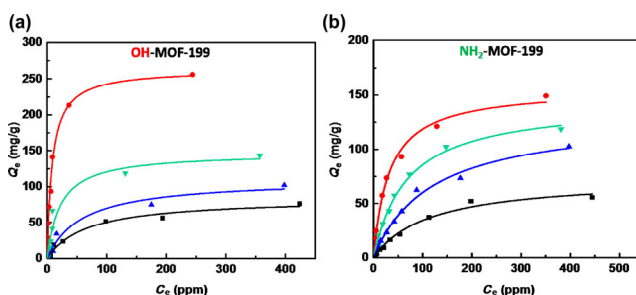
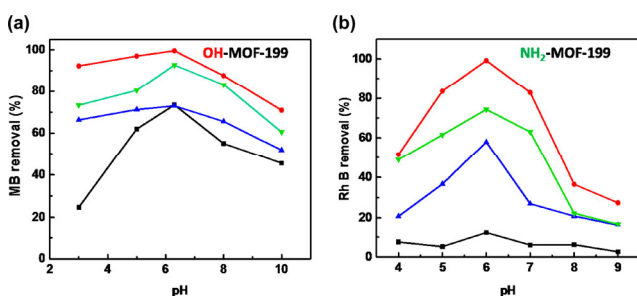


Figure 6 Langmuir adsorption isotherms for OH-BDC:BTC systems (a) and NH₂-BDC:BTC systems (b), respectively: MOF-199 (black), (1:3) (blue), (1:1) (red) and (3:1) (green).

Table 1 Uptake capacity of OH-MOF-199 and NH₂-MOF-199 compared to other adsorbents

Type of adsorbent	Dye	Q _{max} (mg/g)	Reference
Montmorillonite clay	MB	289.12	[52]
Commercial activated carbon	MB	319	[53]
MOF-199/GO	MB	183	[54]
MOF-199	MB	84	This work
OH-MOF-199 (1:1)	MB	263	This work
OH-MOF-199 (3:1)	MB	147	This work
OH-MOF-199 (1:3)	MB	111	This work
Sodium montmorillonite	Rh B	42.19	[55]
Activated carbon	Rh B	16.12	[56]
MIL-125(Ti)	Rh B	180	[57]
MOF-199	Rh B	74	This work
NH ₂ -MOF-199 (1:1)	Rh B	156	This work
NH ₂ -MOF-199 (3:1)	Rh B	143	This work
NH ₂ -MOF-199 (1:3)	Rh B	131	This work

**Figure 7** pH effect on MB and Rh B removal for OH-BDC:BTC systems (a) and NH₂-BDC:BTC systems (b), respectively: MOF-199 (black), (1:3) (blue), (1:1) (red) and (3:1) (green).

for MB and Rh B solutions, respectively. However, for higher pH (7–10), it decreases significantly for Rh B and modestly for MB. In order to understand the mechanism behind these changes, zeta potential measurements of the best performing samples (OH-BDC:BTC (1:1) and NH₂-BDC:BTC (1:1)) are reported in Fig. S7 in the ESM. It is obvious that the surface charge is always negative over a wide range of pH, which explains the adsorption of the positively charged dyes MB and Rh B. More precisely, the surface charge becomes less negative over the acidic range of pH until reaching its peaks coherently with the peak of the uptake. This clearly emphasizes the underlying electrostatic interaction between the positively charged dyes and the negatively charged crystal surfaces. For the higher alkaline pH values, the results differ and the adsorption of Rh B decreases dramatically. This decrease in the uptake can be explained by the fact that Rh B exists in its zwitterion form at this range of pH leading to the formation of dimers that aggregate along with a decrease of its positive charge [58]. For the MB, however, its positive charge is not prominently affected over this pH range leading to a moderate decrease of the uptake. On the other hand, the adsorption of some organic pollutants could be related to the ionic strength because of the electrostatic screening effect [59, 60], which implies that the surface of the MOF becomes more positively charged than in deionized water due to the accumulation of the H⁺ ions from the solution in acidic mediums, thereby rendering an electrostatic repulsion with the positive charge of the dyes and thus decreasing the amount of the adsorbed MB and Rh B. Likewise, at high pH values beyond 6.3, the amount of the dyes adsorbed on the surface of the MOF decreases. This however may be due to the increasing number on Na⁺

ions from the solution, which could compete with the cationic MB and Rh B in their basic forms for the equivalent active adsorption sites in the MOF.

3.5.3 Thermodynamic study: Effect of temperature

To perform a thermodynamic study of the adsorption of MB and Rh B over MOF-199 and its mixed-linker counterparts, adsorption experiments were carried out at four different temperatures: 298, 308, 318, and 328 K. The results for the thermodynamic calculations are shown in Table 2. The thermodynamic parameters of adsorption include the standard enthalpy (ΔH°) in kJ/mol, the standard entropy (ΔS°) in J/(K·mol) and the standard Gibbs free energy (ΔG°) in kJ/mol are extracted from the Van't Hoff plot in accordance to the equations below

$$\Delta G^\circ = \Delta H^\circ - T\Delta S^\circ \quad (4)$$

$$\ln K = (\Delta S^\circ/R) - (\Delta H^\circ/RT) \quad (5)$$

where K is the equilibrium constant, R is the ideal gas constant (8.314 J/(K·mol)).

The positive values of the standard enthalpy ΔH° for MOF-199 and all MTV-MOF systems demonstrate that the adsorption process is endothermic and a stronger interaction exists between pre-adsorbed water and the adsorbent than the interaction between the corresponding dye and the adsorbent which is evident from their high hydrophilic character. The negative values of ΔG° signify the spontaneity of the adsorption process. Furthermore, it is clearly seen that increasing the temperature favors adsorption as ΔG° becomes more negative. Interestingly, the 1:1 ratios for both OH-BDC and NH₂-BDC exhibit the best thermodynamic performance at all temperatures when compared with pure MOF-199 and other MTV-MOFs with different ratios. This provides a thermodynamic interpretation of the relative performance in our adsorption experiments. Moreover, the values of ΔS° , which measure the disorder at the adsorbent/adsorbate interface, exhibit similar trends in Table 2 where the mixed-linker systems (1:1) markedly exhibit the highest ΔS° value as compared to (3:1), (1:3) and pure MOF-199 systems. Such high disorder at the interface seems to play important role in the high affinity of the MOFs towards MB and Rh B in the mixed-linker systems (1:1).

Table 2 Thermodynamic parameters ΔG° (kJ/mol) at four different temperatures, ΔH° (kJ/mol) and ΔS° (J/(K·mol)) for OH-BDC:BTC and NH₂-BDC:BTC systems

Adsorbent	ΔG° (kJ/mol)				ΔH° (kJ/mol)	ΔS° (J/(K·mol))
	T = 298 K	T = 308 K	T = 318 K	T = 328 K		
Methylene blue						
MOF-199	-1.96	-2.25	-2.54	-2.83	7	29
OH-BDC:BTC (1:3)	-1.91	-2.50	-3.10	-3.69	16	60
OH-BDC:BTC (1:1)	-6.38	-9.03	-11.7	-14.3	73	265
OH-BDC:BTC (3:1)	-2.89	-3.55	-4.21	-4.88	17	66
Rhodamine B						
MOF-199	2.04	1.58	1.11	0.65	16	46
NH ₂ -BDC:BTC (1:3)	-1.80	-2.57	-3.33	-4.09	21	76
NH ₂ -BDC:BTC (1:1)	-7.46	-9.16	-10.85	-12.54	43	169
NH ₂ -BDC:BTC (3:1)	-3.06	-3.94	-4.81	-5.69	23	87

3.5.4 Kinetic study

The removal efficiency of MB and Rh B by OH-MOF-199 and NH₂-MOF-199 as a function of contact time is shown in Fig. 8. It can be clearly seen that the highest efficiency and the fastest systems are the ones with 1:1 starting ratios. Linear regression analysis which was performed for two kinetic models: pseudo-first and pseudo-second order (Fig. S8 in the ESM) favors the latter based on the values correlation coefficients for all of the four adsorbents and for both dyes as shown in Table S5 in the ESM. Therefore, the adsorption in our systems is based on a bimolecular reaction mechanism whereby the rate determining step depends on the concentration of both the adsorbent (MOF) and the adsorbate (dye).

Adsorption mechanism: Intra-particle diffusion. In order to gain a better understanding of the adsorption mechanism, the probability of intra-particle diffusion is investigated by applying the following equation

$$q_t = K_p t^{0.5} + C \quad (6)$$

where K_p is the intra-particle diffusion rate constant (mg/(g·min^{1/2})) and C is a constant that defines the boundary layer effect. The graphs in Fig. 9 reveal that the plots are not linear over the entire time interval, though it displays a dual linearity signifying the presence of two consecutive adsorption stages of mass transport with a diminution in the rate. The first stage is the boundary layer effect whereas the second stage refers to the intra-particle diffusion. A linear fit of the second stage permits the estimation of the values of the intra-particle rate constant k and the constant C . It is known that the effect of the intra-particle diffusion is more dominant when the value of C is lower, and when it reaches zero the adsorption process is merely controlled by intra-particle diffusion [53]. However, this is not the case as demonstrated in Fig. 9. It is clear that the linear plot of q_t vs. $t^{1/2}$ of the second part do not pass through the origin and the intercept values are 1.4, 1.5, 3 and 3.5 for MOF-199, OH-BDC:BTC (1:3), OH-BDC:BTC (3:1) and OH-BDC:BTC (1:1), respectively; and 5.8, 6.4 and 9.0 for NH₂-BDC:BTC (1:3), NH₂-BDC:BTC (3:1) and NH₂-BDC:BTC (1:1),

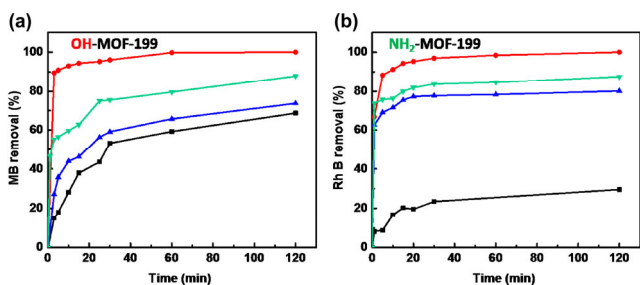


Figure 8 Kinetic curves for MB and Rh B removal as a function of time by OH-BDC:BTC systems (a) and NH₂-BDC:BTC systems (b), respectively: MOF-199 (black), (1:3) (blue), (1:1) (red) and (3:1) (green).

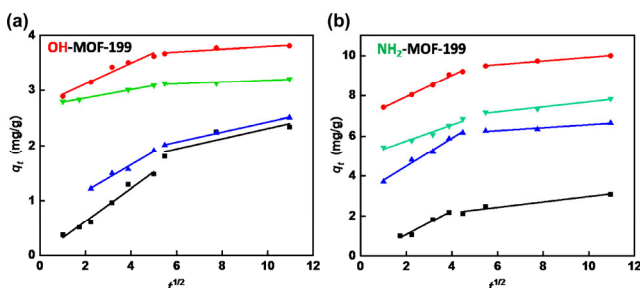


Figure 9 Intra-particle diffusion graphs for OH-BDC:BTC systems (a) and NH₂-BDC:BTC systems (b), respectively: MOF-199 (black), (1:3) (blue), (1:1) (red) and (3:1) (green).

respectively. This indicates that the intra-particle diffusion is not the rate-determining step and is governed by diffusion.

Finally, Fig. 10 shows the recycling capability of OH-BDC:BTC (1:1) and NH₂-BDC:BTC (1:1) for MB and Rh B, respectively for the same adsorption conditions (1 mg of adsorbent/10 mL of 10 ppm dye solution). It is clear from the histograms that both MTV-MOFs systems are recyclable with less than 10% loss in efficiency after three consecutive cycles of adsorption and desorption. Moreover, the desorption process is achieved by stirring the loaded MTV-MOFs in a methanol solution for 30 min. PXRD patterns were also collected after the third cycle of desorption showing an intact crystalline structure for both systems as also shown in Fig. 10.

3.5.5 Selectivity and co-adsorption studies

In order to investigate the specificity of the introduced functional group towards the adsorbed dye, additional experiments were performed on the optimal OH-MOF-199 (1:1) with Rh B and NH₂-MOF-199 (1:1) with MB as well as each system with a equimolar binary solution of MB and Rh B. The results in Fig. 11 demonstrate that while the OH-functionalized MOF-199 adsorbs less Rh B than the NH₂-functionalized MOF-199 and the latter adsorbs MB as good as the OH-functionalized MOF-199. This can be explained by realizing that the MB molecule possesses a sulfur atom which is probably attracted to the metal cation of the adsorbent through acid–base interactions [61] while Rh B is less electron donor due to its stable zwitterion form in solution. On the other hand, the greater affinity of Rh B towards NH₂-MOF-199 might be due to greater hydrogen bonding between the oxygen in Rh B and the amino group of the MOF. In any case, it is noteworthy to first state that the

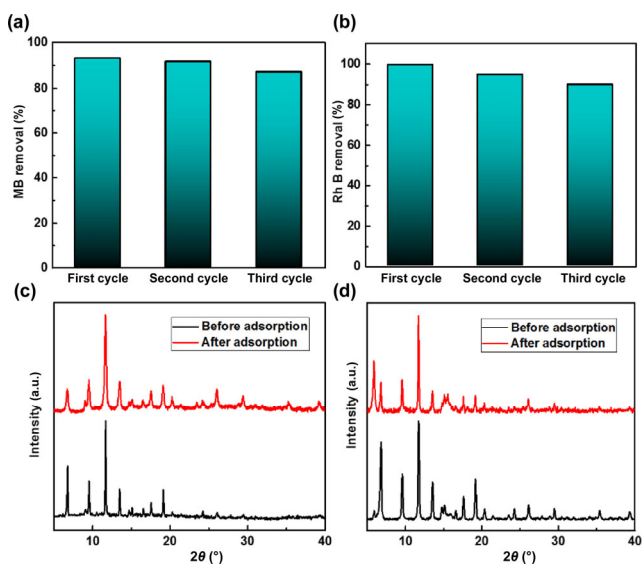


Figure 10 Recycling of OH-BDC:BTC (1:1) (a) and NH₂-BDC:BTC (1:1) (b) and their corresponding PXRD patterns before and after adsorption respectively (c) and (d).

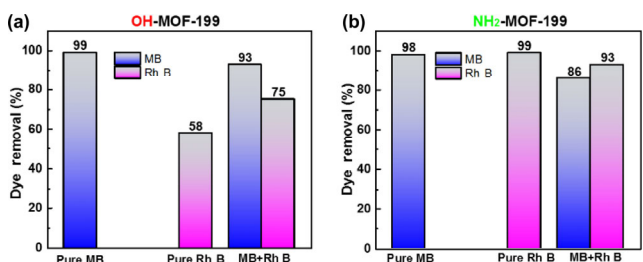


Figure 11 Dye removal percentage from individual and binary solutions of MB and Rh B by each of OH-MOF-199 (a) and NH₂-MOF-199 (b).

defect introduced in the MTV structures enhances the uptake regardless of the functional group when compared to the parent MOF-199 uptake. Hence, the enhanced adsorption obtained is due to the dual effect of introducing the functional group along with the creation of mesopores in the microporous MOF-199 structure allowing for more favorable adsorbent/adsorbate interactions. Moreover, the percentage of dye adsorption from the binary solution of MB and Rh B is higher for both systems which could be associated to the possibility there are newly created disparate specific adsorption sites for each of the dyes on the MTV-MOF, which do not generally compete with each other. These sites are accessible by the dyes, due to their small size, through any pore with a size greater than 1 nm via π - π interactions [62]. This can be seen in Fig. 11 where the adsorption of MB and Rh B in a binary solution is only slightly affected when compared to that in the individual solutions. The slight variations in both panels of Fig. 11 could be due to the interaction of MB and Rh B due to π -stacking of the aromatic rings in a binary solution of the dyes.

4 Conclusion

In this study, MTV-MOF-199 systems were successfully synthesized using a room temperature RDF method. NH_2 -BDC and OH-BDC were incorporated in different ratios into the MOF-199 structure without losing the original crystal structure. A live monitoring of crystal growth and the incorporation progress was recorded throughout the tubular reactor and a full characterization using PXRD, SEM, TGA, BET and NMR of the new systems was performed. Moreover, the new MTV-MOFs were optimal in a 1:1 ratio to enhance the adsorption of MB and Rh B by more than threefold and more than twofold for OH-MOF-199 and NH_2 -MOF-199, respectively compared to MOF-199. The Langmuir adsorption isotherm was found to be the best fit isotherm for both systems with Q_{max} of 263 mg/g for MB and 156 mg/g for Rh B, respectively. The adsorption mechanism was investigated and discussed as well as the recyclability which shows that the MTV-MOFs were easily regenerated for three cycles under our experimental conditions with minor loss in efficiency and a conservation of the crystal structure. Our strategy of introducing defects and functionalities into MOF-199 demonstrates the effectiveness of the heterogeneity within the order to enhance the performance of the MOF adsorbents and their selectivity.

Acknowledgements

We gratefully thank Manal Ammar and Dr. Ali Youssef for their substantial contribution and support. We thank the funding provided by the American University of Beirut Research Board and the K. Shair Central Research Science Laboratory. M. G. acknowledges the support of the Arab Fund Fellowship Program. We also acknowledge the funding provided by the Lebanese National Council for Scientific Research (Nos. 103496 and 103487) and the Masri Institute (No. 103214).

Electronic Supplementary Material: Supplementary material (including the experimental conditions for RDF reactions, PXRD patterns, SEM images, pore size distribution, surface area and pore volume calculated, TGA curves, NMR spectra, FT-IR, zeta potential and UV-Vis adsorption data of the MTV-MOFs-199) is available in the online version of this article at <https://doi.org/10.1007/s12274-020-2870-1>.

References

- Zhou, H. C.; Long, J. R.; Yaghi, O. M. Introduction to metal-organic frameworks. *Chem. Rev.* **2012**, *112*, 673–674.
- McGuire, C. V.; Forgan, R. S. The surface chemistry of metal-organic frameworks. *Chem. Commun.* **2015**, *51*, 5199–217.
- Yaghi, O. M.; O’Keeffe, M.; Ockwig, N. W.; Chae, H. K.; Eddaoudi, M.; Kim, J. Reticular synthesis and the design of new materials. *Nature* **2003**, *423*, 705–714.
- Furukawa, H.; Cordova, K. E.; O’Keeffe, M.; Yaghi, O. M. The chemistry and applications of metal-organic frameworks. *Science* **2013**, *341*, 1230444.
- Furukawa, H.; Ko, N.; Go, Y. B.; Aratani, N.; Choi, S. B.; Choi, E.; Yazaydin, A. Ö.; Snurr, R. Q.; O’Keeffe, M.; Kim, J. et al. Ultrahigh porosity in metal-organic frameworks. *Science* **2010**, *329*, 424–428.
- Rojas, S.; Carmona, F. J.; Maldonado, C. R.; Horcajada, P.; Hidalgo, T.; Serre, C.; Navarro, J. A. R.; Barea, E. Nanoscaled zinc pyrazolate metal-organic frameworks as drug-delivery systems. *Inorg. Chem.* **2016**, *55*, 2650–2663.
- Zhao, D.; Cui, Y. J.; Yang, Y.; Qian, G. D. Sensing-functional luminescent metal-organic frameworks. *CrystEngComm* **2016**, *18*, 3746–3759.
- Yang, X. C.; Xu, Q. Bimetallic metal-organic frameworks for gas storage and separation. *Ryst. Growth Des.* **2017**, *17*, 1450–1455.
- Xiong, G.; Yu, B.; Dong, J.; Shi, Y.; Zhao, B.; He, L. N. Cluster-based MOFs with accelerated chemical conversion of CO_2 through C–C bond formation. *Chem. Commun.* **2017**, *53*, 6013–6016.
- Stock, N.; Biswas, S. Synthesis of metal-organic frameworks (MOFs): Routes to various MOF topologies, morphologies, and composites. *Chem. Rev.* **2012**, *112*, 933–969.
- Kreno, L. E.; Leong, K.; Farha, O. K.; Allendorf, M.; Van Duyne, R. P.; Hupp, J. T. Metal-organic framework materials as chemical sensors. *Chem. Rev.* **2012**, *112*, 1105–1125.
- Belmabkhout, Y.; Guillerm, V.; Eddaoudi, M. Low concentration CO_2 capture using physical adsorbents: Are metal-organic frameworks becoming the new benchmark materials? *Chem. Eng. J.* **2016**, *296*, 386–397.
- Issa, R.; Hmadeh, M.; Al-Ghoul, M. Control of particle size and morphology of MOF-199 crystals via a reaction-diffusion framework. *Defect Diffus. Forum* **2017**, *380*, 39–47.
- Zhu, H. L.; Liu, D. X. The synthetic strategies of metal-organic framework membranes, films and 2D MOFs and their applications in devices. *J. Mater. Chem. A* **2019**, *7*, 21004–21035.
- Sun, D. R.; Sun, F. X.; Deng, X. Y.; Li, Z. H. Mixed-metal strategy on metal-organic frameworks (MOFs) for functionalities expansion: Co substitution induces aerobic oxidation of cyclohexene over inactive Ni-MOF-74. *Inorg. Chem.* **2015**, *54*, 8639–8643.
- Villajos, J. A.; Orcajo, G.; Martos, C.; Botas, J. Á.; Villacañas, J.; Calleja, G. Co/Ni mixed-metal MOF-74 material as hydrogen adsorbent. *Int. J. Hydrogen Energy* **2015**, *40*, 5346–5352.
- Naeem, A.; Ting, V. P.; Hintermair, U.; Tian, M.; Telford, R.; Halim, S.; Nowell, H.; Holyńska, M.; Teat, S. J.; Scowen, I. J. et al. Mixed-linker approach in designing porous zirconium-based metal-organic frameworks with high hydrogen storage capacity. *Chem. Commun.* **2016**, *52*, 7826–7829.
- Haldar, R.; Maji, T. K. Metal-organic frameworks (MOFs) based on mixed linker systems: Structural diversities towards functional materials. *CrystEngComm* **2013**, *15*, 9276–9295.
- Deng, H. X.; Doonan, C. J.; Furukawa, H.; Ferreira, R. B.; Towne, J.; Knobler, C. B.; Wang, B.; Yaghi, O. M. Multiple functional groups of varying ratios in metal-organic frameworks. *Science* **2010**, *327*, 846–850.
- Kong, X. Q.; Deng, H. X.; Yan, F. Y.; Kim, J.; Swisher, J. A.; Smit, B.; Yaghi, O. M.; Reimer, J. A. Mapping of functional groups in metal-organic frameworks. *Science* **2013**, *341*, 882–885.
- Qin, J. S.; Yuan, S.; Wang, Q.; Alsalmeh, A.; Zhou, H. C. Mixed-linker strategy for the construction of multifunctional metal-organic frameworks. *J. Mater. Chem. A* **2017**, *5*, 4280–4291.
- Osborn Popp, T. M.; Yaghi, O. M. Sequence-dependent materials. *Acc. Chem. Res.* **2017**, *50*, 532–534.
- Lee, Y.; Kim, S.; Kang, J. K.; Cohen, S. M. Photocatalytic CO_2 reduction by a mixed metal (Zr/Ti), mixed ligand metal-organic framework under visible light irradiation. *Chem. Commun.* **2015**, *51*, 5735–5738.
- Duan, C. Z.; Li, F. E.; Zhang, H.; Li, J. Q.; Wang, X. J.; Xi, H. X. Template synthesis of hierarchical porous metal-organic frameworks with tunable porosity. *RSC Adv.* **2017**, *7*, 52245–52251.

- [25] Shi, Z. N.; Li, L.; Xiao, Y. X.; Wang, Y. X.; Sun, K. K.; Wang, H. X.; Liu, L. Synthesis of mixed-ligand Cu–MOFs and their adsorption of malachite green. *RSC Adv.* **2017**, *7*, 30904–30910.
- [26] Peterson, G. W.; Au, K.; Tovar, T. M.; Epps, T. H. Multivariate CuBTC metal–organic framework with enhanced selectivity, stability, compatibility, and processability. *Chem. Mater.* **2019**, *31*, 8459–8465.
- [27] Yuan, S.; Qin, J. S.; Li, J. L.; Huang, L.; Feng, L.; Fang, Y.; Lollar, C.; Pang, J. D.; Zhang, L. L.; Sun, D. et al. Retrosynthesis of multi-component metal–organic frameworks. *Nat. Commun.* **2018**, *9*, 808.
- [28] Furukawa, H.; Müller, U.; Yaghi, O. M. “Heterogeneity within order” in metal–organic frameworks. *Angew. Chem., Int. Ed.* **2015**, *54*, 3417–3430.
- [29] Burrows, A. D. Mixed-component metal–organic frameworks (MC-MOFs): Enhancing functionality through solid solution formation and surface modifications. *CrystEngComm* **2011**, *13*, 3623–3642.
- [30] Wang, L. J.; Deng, H. X.; Furukawa, H.; Gándara, F.; Cordova, K. E.; Peri, D.; Yaghi, O. M. Synthesis and characterization of metal–organic framework-74 containing 2, 4, 6, 8, and 10 different metals. *Inorg. Chem.* **2014**, *53*, 5881–5883.
- [31] Ayoub, G.; Karadeniz, B.; Howarth, A. J.; Farha, O. K.; Đilović, I.; Germann, L. S.; Dinnebier, R. E.; Užarević, K.; Friscic, T. Rational synthesis of mixed-metal microporous metal–organic frameworks with controlled composition using mechanochemistry. *Chem. Mater.* **2019**, *31*, 5494–5501.
- [32] Karagiari, O.; Bury, W.; Mondloch, J. E.; Hupp, J. T.; Farha, O. K. Solvent-assisted linker exchange: An alternative to the *de novo* synthesis of unattainable metal–organic frameworks. *Angew. Chem., Int. Ed.* **2014**, *53*, 4530–4540.
- [33] Xi, W. Q.; Liu, Y.; Xia, Q. C.; Li, Z. J.; Cui, Y. Direct and post-synthesis incorporation of chiral metallosalen catalysts into metal–organic frameworks for asymmetric organic transformations. *Chem.—Eur. J.* **2015**, *21*, 12581–12585.
- [34] Yuan, S.; Lu, W. G.; Chen, Y. P.; Zhang, Q.; Liu, T. F.; Feng, D. W.; Wang, X.; Qin, J. S.; Zhou, H. C. Sequential linker installation: Precise placement of functional groups in multivariate metal–organic frameworks. *J. Am. Chem. Soc.* **2015**, *137*, 3177–3180.
- [35] Chen, C. X.; Wei, Z. W.; Jiang, J. J.; Fan, Y. Z.; Zheng, S. P.; Cao, C. C.; Li, Y. H.; Fenske, D.; Su, C. Y. Precise modulation of the breathing behavior and pore surface in Zr-MOFs by reversible post-synthetic variable-spacer installation to fine-tune the expansion magnitude and sorption properties. *Angew. Chem., Int. Ed.* **2016**, *55*, 9932–9936.
- [36] Li, T.; Sullivan, J. E.; Rosi, N. L. Design and preparation of a core–shell metal–organic framework for selective CO₂ capture. *J. Am. Chem. Soc.* **2013**, *135*, 9984–9987.
- [37] He, L. C.; Liu, Y.; Liu, J. Z.; Xiong, Y. S.; Zheng, J. Z.; Liu, Y. L.; Tang, Z. Y. Core–shell noble-metal@metal-organic-framework nanoparticles with highly selective sensing property. *Angew. Chem., Int. Ed.* **2013**, *125*, 3829–3833.
- [38] Tranchemontagne, D. J.; Hunt, J. R.; Yaghi, O. M. Room temperature synthesis of metal-organic frameworks: MOF-5, MOF-74, MOF-177, MOF-199, and IRMOF-0. *Tetrahedron* **2008**, *64*, 8553–8557.
- [39] Al-Ghoul, M.; Issa, R.; Hmadeh, M. Synthesis, size and structural evolution of metal–organic framework-199 via a reaction–diffusion process at room temperature. *CrystEngComm* **2017**, *19*, 608–612.
- [40] Zhuang, J. L.; Ceglarek, D.; Pethuraj, S.; Terfort, A. Rapid room-temperature synthesis of metal–organic framework HKUST-1 crystals in bulk and as oriented and patterned thin films. *Adv. Funct. Mater.* **2011**, *21*, 1442–1447.
- [41] Al Akhrass, G. A.; Ammar, M.; El-Rassy, H.; Al-Ghoul, M. Self-assembled lanthanum hydroxide microspheres within a reaction-diffusion framework: Synthesis, characterization, control and application. *RSC Adv.* **2016**, *6*, 3433–3439.
- [42] Saliba, D.; Ezzeddine, A.; Emwas, A. H.; Khashab, N. M.; Al-Ghoul, M. Dynamics and mechanism of intercalation/de-intercalation of rhodamine B during the polymorphic transformation of the CdAl layered double hydroxide to the brucite-like cadmium hydroxide. *Ryst. Growth Des.* **2016**, *16*, 4327–4335.
- [43] Saliba, D.; Ezzeddine, A.; Sougrat, R.; Khashab, N. M.; Hmadeh, M.; Al-Ghoul, M. Cadmium–aluminum layered double hydroxide microspheres for photocatalytic CO₂ reduction. *ChemSusChem* **2016**, *9*, 800–805.
- [44] Rahbani, J.; Ammar, M.; Al-Ghoul, M. Reaction-diffusion framework: The mechanism of the polymorphic transition of α - to β -cobalt hydroxide. *J. Phys. Chem. A* **2013**, *117*, 1685–1691.
- [45] Saliba, D.; Al-Ghoul, M. Stability and particle size control of self-assembled cadmium–aluminum layered double hydroxide. *CrystEngComm* **2016**, *18*, 8445–8453.
- [46] Saliba, D.; Ammar, M.; Rammal, M.; Al-Ghoul, M.; Hmadeh, M. Crystal growth of ZIF-8, ZIF-67, and their mixed-metal derivatives. *J. Am. Chem. Soc.* **2018**, *140*, 1812–1823.
- [47] Redfield, P. Fluid technologies: The Bush Pump, the LifeStraw® and microworlds of humanitarian design. *Soc. Stud. Sci.* **2016**, *46*, 159–183.
- [48] Eddouadi, M.; Kim, J.; Wachter, J.; Chae, H. K.; O’keeffe, M.; Yaghi, O. M. Porous metal–organic polyhedra: 25 Å cuboctahedron constructed from 12 Cu₂(CO₃)₄ paddle-wheel building blocks. *J. Am. Chem. Soc.* **2001**, *123*, 4368–4369.
- [49] Venna, S. R.; Jasinski, J. B.; Carreon, M. A. Structural evolution of zeolitic imidazolate framework-8. *J. Am. Chem. Soc.* **2010**, *132*, 18030–18033.
- [50] Fang, Z. L.; Dürholt, J. P.; Kauer, M.; Zhang, W. H.; Lochenie, C.; Jee, B.; Albada, B.; Metzler-Nolte, N.; Pöpl, A.; Weber, B. et al. Structural complexity in metal–organic frameworks: Simultaneous modification of open metal sites and hierarchical porosity by systematic doping with defective linkers. *J. Am. Chem. Soc.* **2014**, *136*, 9627–9636.
- [51] Park, J.; Wang, Z. U.; Sun, L. B.; Chen, Y. P.; Zhou, H. C. Introduction of functionalized mesopores to metal–organic frameworks via metal–ligand–fragment coassembly. *J. Am. Chem. Soc.* **2012**, *134*, 20110–20116.
- [52] Xiong, L.; Yang, Y.; Mai, J. X.; Sun, W. L.; Zhang, C. Y.; Wei, D. P.; Chen, Q.; Ni, J. R. Adsorption behavior of methylene blue onto titanate nanotubes. *Chem. Eng. J.* **2010**, *156*, 313–320.
- [53] Raposo, F.; De La Rubia, M. A.; Borja, R. Methylene blue number as useful indicator to evaluate the adsorptive capacity of granular activated carbon in batch mode: Influence of adsorbate/adsorbent mass ratio and particle size. *J. Hazard. Mater.* **2009**, *165*, 291–299.
- [54] Li, L.; Liu, X. L.; Geng, H. Y.; Hu, B.; Song, G. W.; Xu, Z. S. A MOF/graphite oxide hybrid (MOF: HKUST-1) material for the adsorption of methylene blue from aqueous solution. *J. Mater. Chem. A* **2013**, *1*, 10292–10299.
- [55] Selvam, P. P.; Preethi, S.; Basakaralingam, P.; Thinakaran, N.; Sivasamy, A.; Sivanesan, S. Removal of rhodamine B from aqueous solution by adsorption onto sodium montmorillonite. *J. Hazard. Mater.* **2008**, *155*, 39–44.
- [56] Kadirvelu, K.; Karthika, C.; Vennilamani, N.; Pattabhi, S. Activated carbon from industrial solid waste as an adsorbent for the removal of rhodamine-B from aqueous solution: Kinetic and equilibrium studies. *Chemosphere* **2005**, *60*, 1009–1017.
- [57] Guo, H. X.; Lin, F.; Chen, J. H.; Li, F. M.; Weng, W. Metal–organic framework MIL-125(Ti) for efficient adsorptive removal of rhodamine B from aqueous solution. *Appl. Org. Chem.* **2015**, *29*, 12–19.
- [58] Eftekhari, S.; Habibi-Yangjeh, A.; Sohrabnezhad, S. Application of AIMCM-41 for competitive adsorption of methylene blue and rhodamine B: Thermodynamic and kinetic studies. *J. Hazard. Mater.* **2010**, *178*, 349–355.
- [59] Dukhin, S. J. Lyklema (Ed.). Fundamentals of Interface and Colloid Science, vol. IV, Academic Press, New York-Toronto (2005). *Adv. Colloid Interface Sci.* **2006**, *119*, 69–70.
- [60] Fontecha-Cámara, M. A.; López-Ramón, M. V.; Álvarez-Merino, M. A.; Moreno-Castilla, C. Effect of surface chemistry, solution pH, and ionic strength on the removal of herbicides diuron and amitrole from water by an activated carbon fiber. *Langmuir* **2007**, *23*, 1242–1247.
- [61] Blanco-Brieva, G.; Campos-Martin, J. M.; Al-Zahrani, S. M.; Fierro, J. L. G. Removal of refractory organic sulfur compounds in fossil fuels using MOF sorbents. *Global Nest J.* **2010**, *12*, 296–304.
- [62] Banerjee, A.; Gokhale, R.; Bhatnagar, S.; Jog, J.; Bhardwaj, M.; Lefez, B.; Hannyer, B.; Ogale, S. MOF derived porous carbon–Fe₃O₄ nanocomposite as a high performance, recyclable environmental superadsorbent. *J. Mater. Chem.* **2012**, *22*, 19694–19699.